Determination of weather-induced short-term sea level variations by GNSS reflectometry

Théo Gravalon, Lucía Seoane, Guillaume Ramillien, José Darrozes, Laurent Roblou

Version of Record: https://www.sciencedirect.com/science/article/pii/S0034425722002048
Manuscript_de66c490481cdc01d5b63c5efc9a9e33

Determination of weather-induced short-term sea level variations by GNSS reflectometry

Théo Gravalon[a,b,*], Lucía Seoane[a,b], Guillaume Ramillien[a,c], José Darrozes[a,b], Laurent Roblou[c,d]

[a] *Géosciences Environnement Toulouse (GET), France*
[b] *Université Paul Sabatier (UPS), France*
[c] *Centre National de la Recherche Scientifique (CNRS), France*
[d] *Laboratoire d'Aérologie (LAERO), France*

Abstract

We propose to derive local sea level variations by using the Signal-to-Noise Ratio (SNR) of the GNSS reflected signals at four GNSS single antenna sites (ILDG, TAR0, FFT2, LYTT) located at different latitudes. For these sites representing various ocean conditions (waves, tides, storm surges, etc...), tides estimates by SNR are highly consistent to tide gauges records as highlighted by tidal harmonic analysis, with a Root-Sum-Square (RSS) ranging from few centimeter in micro-tidal environment to near a decimeter in macro-tidal environment.SNR non-tidal residuals (NTR) are compared to two modelled sea level responses to meteorological forcing, namely the analytical Local Inverse Barometer (LIB) model and the numerical Dynamic Atmospheric Correction (DAC). Both DAC and LIB models are coherent with this non-tidal SNR residual in a 2-days to 2-months time window with correlations reaching 0.7 and high coherences. Several noteworthy atmospheric events are observed in the time series of about one year. During intense events, SNR and models are highly correlated. According to the results obtained in this study, we conclude that the GNSS reflectometry technique is relevant to derive sea level variations at tidal periods but also for studying the behaviour of the sea surface in response to atmospheric forcing at short-term scales.

Index terms— GNSS-R, Coastal sea level, Meteorological forcing, Storm surges

1. INTRODUCTION

Sea Surface Height (SSH, Gregory et al. (2019)) are largely studied by different techniques such as tide gauges (e.g.Ponte et al. (2019)), conventional satellite altimetry (e.g. Ablain et al. (2017)), SAR satellite altimetry (e.g. Anzidei et al. (2021)) or a combination of some of these methods (e.g. Meli et al. (2021)). At long-term temporal scales, sea height variations are an important indicator of sea-level rise due to Global Warming (Shukla et al., 2017). At higher frequencies, from monthly to sub-daily timescales, the sea level observations allow the monitoring of ocean tides, waves and the response to atmospheric forcing. In coastal zones, important phenomena with a big impact on society and ecosystems act, as erosion or oceanic surges. However, in these near-shore areas satellite altimetry observations remain imprecise (Vignudelli et al., 2005; Cipollini et al., 2017) and tide gauge coverage remains sparse (Melet et al., 2020), challenging the understanding of contemporary sea level changes (Ponte et al., 2019). For this purpose, GNSS Reflectometry

(GNSS-R) has been developed in the last decades as an opportunistic method based on the study of the reflected electromagnetic signals reaching a GNSS antenna. Previous studies (Roussel et al., 2015; Löfgren et al., 2014; Tabibi et al., 2020; Geremia-Nievinski et al., 2020; Chen et al., 2019) have shown the good performance of the GNSS-R technique to observe tidal variations in sea level. This technique presents several advantages. When collocated to a tide gauge, it provides redundancy and thus, acts as a complement to the tide gauge estimates (in case of measurement interruption). The combination of both could allow a better characterization of sea level in coastal areas. On the other hand, the GNSS-R represents an opportunistic and self-sufficient technique of sea surface height measurement, based on pre-existing GNSS station networks such as in polar regions (Tabibi et al., 2020). We use the GNSS reflectometry in this point of view to assess its capability in measuring sea level variations beyond the tides.

Besides tides, winds and atmospheric pressure variations cause significant changes in sea height (Woodworth et al., 2019). At scales of several days, most of the sea level variability comes from atmospheric forcing, i.e, the response of the sea surface to atmospheric pressure variations and wind (Woodworth et al., 2019). A first approximation of the sea level response to this forcing has been understood for more than a century. Some of the first observations were made by Ross (1854) using a mercury barometer (Roden and Rossby, 1999), leading to the Inverse Barometer (IB) effect theory. The Local (LIB) theory states that sea level variations are directly linked to pressure variations by a coefficient of $\sim 1\,\mathrm{cm} \cdot \mathrm{hPa}^{-1}$(Ponte et al., 1991; Ponte, 1993). This theory is applicable for periods larger than two days (Ponte et al., 1991). Several studies (Wunsch and Stammer, 1997; Mathers and Woodworth, 2001) have shown the variation of this coefficient is weaker in the tropical band. However, this static response of the ocean to atmospheric pressure variations is vanishing for periods less than 20 days where the dynamic character of the ocean response to atmospheric pressure forcing and the wind forcing are preponderant (Carrère and Lyard, 2003). To take this into account, the Dynamic Atmospheric Correction (DAC) has been developed (Carrère, 2003; Carrere et al., 2016) as a combination of the IB response at periods longer than 20 days, and a barotropic model of the dynamic ocean response to atmospheric wind and pressure forcing for periods less than 20 days. The difference between the DAC and the LIB at high frequencies can be observed in Figure 1.

The signature of the atmospheric forcing has been observed by GNSS-R with a focus on singular site studies (extreme events as storms and typhoons Vu et al. (2019); Peng et al. (2019)), and a further evaluation of this capability is still needed. The main goal of this paper is to extend these case studies for longer durations and thus, evaluate the performance of GNSS-R for measuring sea surface variations caused by short-term meteorological forcing around the world in different configurations.

For this study, the four observation sites used are first presented. They have been chosen to represent different latitudes and environmental conditions. Secondly, the data and models are described. Thirdly, we introduce the Signal-to-Noise Ratio (SNR) GNSS-R method to obtain SSH. Fourth, we compare SSH derived

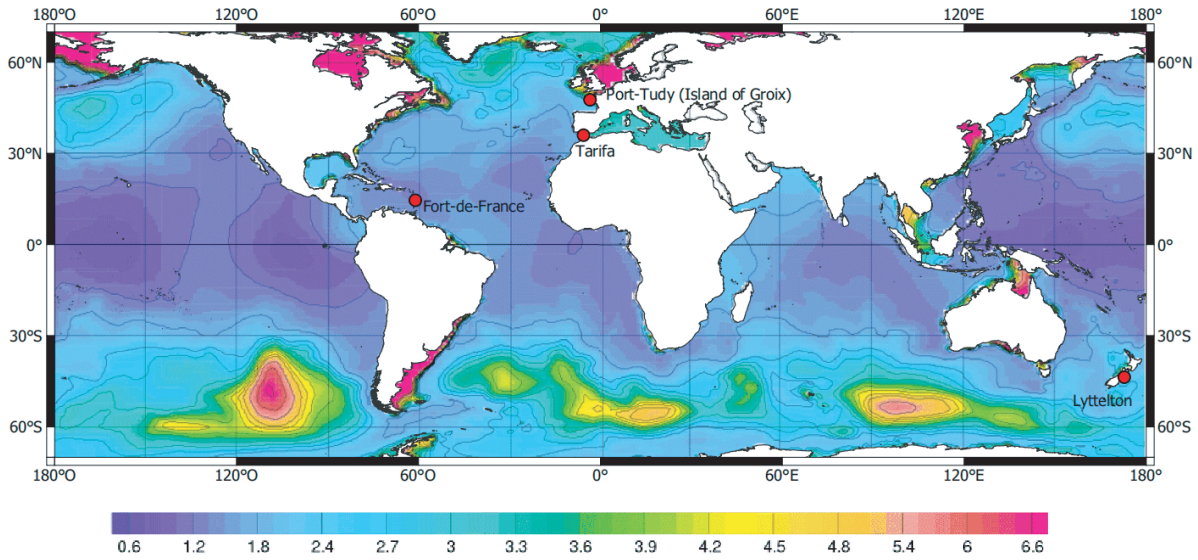

Figure 1: Location of the different sites along with Root Mean Square of the Inverse Barometer departure (difference between the model output and a inverse barometer approximation) obtained with the DAC barotropic model MOG2D forced by pressure and wind at high frequencies (0.5-20 days) in centimeters (Carrère, 2003)

from GNSS-R to tides gauges measurements through a harmonic analysis as a first validation step of the GNSS-R processing method. Finally we analyze the physical content of non-tidal residuals. This latter is compared to a sea surface response computed using LIB and DAC models.

2. SITES LOCATIONS

Colocated GNSS antennas and tide gauges are necessary to quantify the performance and the reliability of the proposed methodology. Four sites have been chosen at different latitudes (Figure 1): Port Tudy at Groix Island in France (ILDG) , Tarifa in Spain (TAR0), Fort-de-France in French Island of Martinique (FFT2) and Lyttelton in New Zealand (LYTT). The description of sites are shown in Table 1. In addition, these sites have different tidal ranges: macrotidal for ILDG (∼5.7 m); mesotidal for LYTT (∼3.2 m); microtidal for TAR0 (∼1.5 m) and FFT2 (∼0.7 m).

Two factors have been important in our site choice: the geographical configuration and the meteorological conditions. A nearly one year period is defined for all sites (2018-2020 depending on the site). This time span is suited for the observations of atmospherically-driven sea level variations which are ranging from daily (wind-driven and dynamic response) to monthly scales (static LIB response).

Concerning the first site, ILDG directly faces the oceanic waters, TAR0 is located at the transition between the Atlantic ocean and the Mediterranean sea in a protected harbour, i.e protected from waves and wind, FFT2 is situated in a city harbour in the tropical band and LYTT is located in one of the biggest bay in the Banks peninsula.

Relating to the meteorological conditions, the ILDG and TAR0 sites are situated in a region affected by the European windstorm season associated with high barometric variations and wind. A period of higher intensity storms occurred in December 2019 affecting Spain and the bay of Biscay (Elsa and Fabien storms). For FFT2, the tropical storm Dorian in August 2019 was a major event that hit Martinique Island (later classified as a class-5 hurricane). For LYTT, the focus is made on the Fehi storm (01/02/2018) which was responsible for casualties in southern New Zealand.

3. DATA

3.1. GNSS

The GNSS observations of ILDG, FFT2, TAR0 and LYTT are provided by the Service d'Observation du Niveau des Eaux Littorales (SONEL Wöppelmann (2004)) as a part of the Global Sea Level Observing System (GLOSS, Woodworth (1991)). Each data-set is available in RINEX format with a sampling rate of 30 seconds. GPS and GLONASS constellations are considered. For both constellations, SNR from both the L1 (C/A code) and legacy L2 (P(Y) code) are used. The sampling rate of 30-second of the RINEX data set is enough to process properly the data for each sites. Actually Santamaría-Gómez et al. (2015) gives a theoretical maximum antenna height of about 13 meters while processing 30 seconds RINEX with both L1 and L2. This treshold value is above all of our antenna heights (the maximum height in our study areas being 8.5 meters at TAR0).

The ILDG and FFT2 stations are part of the French permanent GNSS network (RGP). The TAR0 station belongs to the ERGNSS (Red Geodésica Nacional de Estaciones de Referencia GNSS, Spain) and the EUREF permanent Network. The LYTT station is operated by the Otago University. More detailed information about the four GNSS stations are given in Table 1.

3.2. Tide gauges

Data from the tide gauges are made available by the GLOSS organizations, the Permanent Service for Mean Sea Level and the University of Hawaii Sea Level Center (UHSLC). In the case of French sites, ILDG and FFT2, the tide gauges are part of the Réseau d'Observation du NIveau de la Mer. This network is operated by the Service d'Hydrographie de la Marine. Both tide gauges are Krohne radar type sensors (Voineson, 2013) located in a stilling well. The measurement sampling rate is one minute.

For the Spanish site, TAR0, the sea level observations are issued from a miros radar tide gauge (García and Molinero, 2006) which is part of REDMAR network (Pérez et al., 2014). The raw measurements are retrieved from the Joint Research Center database (JRC, Remus et al. (2010)) and they are provided with a sampling of 5 minutes. Finally the tide gauge at LYTT site is operated by the Lyttelton harbour authority. The data are made available by the UHSLC with a sampling period of one hour. At all sites, tide gauges and GNSS stations are collocated with a horizontal distance ranging from less than 1 m (LYTT) to about 300 m (TAR0).

Site	Latitude	Longitude	h0 h1	Antenna Type	GNSS Receiver Type	Obs. Period	dL	dH	Azimut Mask [°]	Elevation Mask [°]
ILDG	47°38'40"	-3°26'45"	6.8 56.2	Topcon CR-G5	Spectra SP90M	20/02/19 to 31/12/19	15	5.7	20/110	0/16
TAR0	36°0'31"	-5°36'10"	8.5 50.1	Leica AR20	Leica GR25	17/07/19 to 15/07/20	307	1.6	290/240	5/18
FFT2	14°36'05"	-61°03'48"	8.0 -29.9	Leica AR20	Leica GR25	18/04/19 to 30/04/20	53	0.7	130/260	5/25
LYTT	-43°36'21"	172°43'20"	6.6 18.4	Leica AT504	Leica GRX1200	01/01/18 to 16/12/18	1	3.2	120/250	5/25

Table 1: GNSS-R sites detailed informations. Azimuth expressed in clockwise direction; h0: Reflector depth above mean sea level [m], h1: Station ellipsoidal height [m], dL: the distance to the tide gauge [m], dH: tidal range [m]

3.3. Atmospheric Pressure

Atmospheric pressure observations near ILDG, FFT2 and TAR0 are provided by Infoclimat (`https://www.infoclimat.fr` last access on the 13/12/21) with a sampling of 1 hour. For the French sites, these measurements are issued from METeorological Aerodrome Report (METAR) stations operated by Meteo-France. Distances between GNSS and weather stations are 13 km, 7.5 km and 1 km for ILDG, FFT2 and TAR0 respectively.

The atmospheric pressure data at LYTT site are available from the Lyttelton Port Company (`https://www.lpc.co.nz`) with one-minute sampling and are located in the same harbour as the GNSS antenna and tide gauge.

3.4. Dynamic atmospheric correction

The DAC is computed by combining the LIB approximation of $1\,\mathrm{cm}\cdot\mathrm{hPa}^{-1}$ at low frequencies (periods exceeding 20 days) and the barotropic model Mog2D-G outputs (Carrère and Lyard, 2003; Carrere et al., 2016) at high frequencies (periods less than 20 days). The Mog2D model is forced by air pressure and wind derived from ECMWF products. The differences between Mog2D and the LIB approximation are represented in Figure 1. The DAC is produced by CLS (Collecte Localisation Satellites, Toulouse, France) and distributed by Aviso + (https://www.aviso.altimetry.fr) supported by Centre National d'Etudes Spatiales. These fields are provided every 6 hours over a global grid of 0.25 degrees ($\sim$ 28 km) of spatial resolution.

The DAC is commonly used for correcting satellite altimetry data. It is adapted to study the high frequency response of the sea level as the ocean signal is mostly barotropic (Vinogradova et al., 2007), whereas the LIB presents several drawbacks due to the dynamical response of the sea and non-consideration

of the wind, which is predominant around the 10-day period (Carrère and Lyard, 2003), in particular in coastal areas (Woodworth et al., 2019; Ding et al., 2011; Lyard and Roblou, 2003).

The DAC and to a lower extent, the LIB are the principal solutions providing a modeled response of the sea surface to meteorological forcing. They are fully uncorrelated from other sea level forcing factors (i.e. seiches, ocean circulation, waves, and so on).

4. METHODOLOGY

4.1. SSH derived from GNSS-R

The GNSS SNR quantify the quality of the signal received on an antenna. The energy of the GNSS signal is due to the combination of the direct and reflected signals which contribute to the shape of the SNR. The SNR data is available in the RINEX files provided by the GNSS receivers in dB.Hz. The amplitude of the direct signal, A_d, is considered largely superior to the reflected signal amplitude A_r, because the coherent amplitude is reduced by scattering on rough surfaces and through the geodetic antennas design (Smyrnaios et al., 2013). Then, the square SNR norm is approximated by (Larson et al., 2008):

$$SNR \approx A_d^2 + 2A_dA_r \cos\psi \tag{1}$$

where ψ is the phase difference between the direct and the reflected signals. Supposing a horizontal reflector surface and specular reflections, ψ is estimated as a geometrical function of the path delay of the reflected signal, δ (Bishop et al., 1985) :

$$\psi = \frac{2\pi}{\lambda}\delta = \frac{4\pi h}{\lambda}\sin\epsilon \tag{2}$$

with λ the wavelength (in m), ϵ the elevation angle of the satellite (in °) w.r.t the antenna's plane horizon and h the vertical height (in m) between the antenna phase center and the reflecting surface (see Figure 2). Deriving Equation 2 with time t, the multipath frequency oscillation is obtained as (Roussel et al., 2015):

$$\tilde{f} = \frac{\mathrm{d}\psi}{\mathrm{d}x} = \frac{4\pi}{\lambda}\left(\dot{h}\frac{\tan\epsilon}{\dot{\epsilon}} + h\right) \tag{3}$$

with $x = \sin\epsilon$ and $\dot{h} = \mathrm{d}h/\mathrm{d}t$ the sea level vertical variation speed (in m/s). In practice, a second-order polynomial function is adjusted from raw SNR data in order to remove the direct signal contribution (Larson et al., 2013; Roussel et al., 2015). The residual SNR presents a periodical behavior based on the multipath frequency. A Lomb Scargle Periodogram (Lomb, 1976) is then applied to the residuals to estimate the position $\tilde{f}$ of the maximum peak of the residual SNR spectrum. Finally, following this detection, a $\tilde{f}_k$ is determined for each satellite k during a $2{\cdot}\delta t$ integration-time window centered on a given epoch i. δt has to be optimized to reach the best results when observing the tides according to Roussel et al. (2015). Using Equation 3, h^i and $\dot{h}^i$ are adjusted by Least Square Method (Figure 2). In this study, h^i is determined with a sampling of $\Delta t = 5$ minutes for deriving a GNSS-R sea level variation time series.

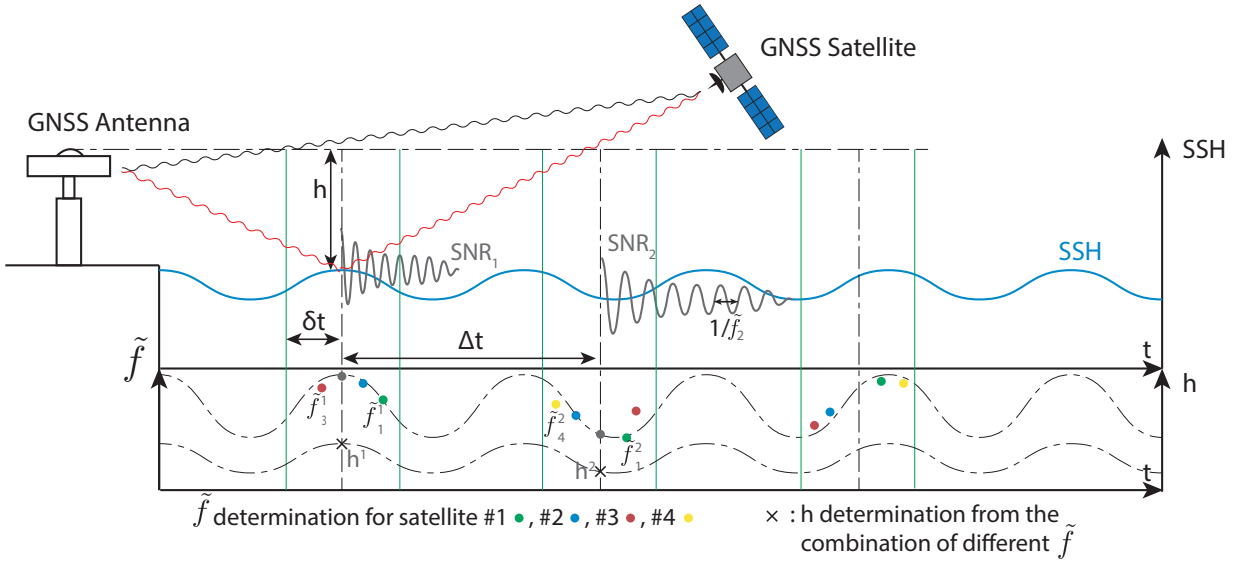

Figure 2: Principle of the SNR based method to retrieve sea level height h. The sea level variations is represented in blue, and the corresponding detrended SNR at a given epoch in red. Inspired from Roussel et al. (2015) and Santamaría-Gómez et al. (2015).

The simulator earlier proposed by Roussel et al. (2014) is used in order to avoid reflections located over land, pier, buildings, etc. Masks depending on azimuth and elevation values are created to keep the appropriated reflection points in the h adjustment process (Figure 3 and Table 1).

As the GNSS-R technique is based on GNSS signals, it suffers from the impact of the atmosphere, especially from the impact of the troposphere creating tropospheric delays. These delays generate biases in the GNSS-R estimates, leading to an underestimation of the height between the reflection surfaces and the antenne. In the case of a moving reflection surface, it creates a scaling factor between the true reflector height and the GNSS-R estimates (Williams and Nievinski, 2017; Peng et al., 2019). The correction of these delays improves the accuracy of the estimates with respect to tide gauges records (Santamaría-Gómez and Watson, 2017; Williams and Nievinski, 2017; Larson et al., 2017).

Due to the scaling factor theory, the errors caused by tropospheric delays alter the tides amplitude recovery, however they poorly affect the non-tidal residuals of less than 1 meter. As the retrieval of tides is not the main purpose of our study, but the analysis of the non-tidal residual, no tropospheric delays corrections are applied here.

4.2. Non-Tidal Residual (NTR) processing and analysis methods

The time series of GNSS-R SSH with tides removed is called the Non-Tidal Residual (NTR Gregory et al. (2019)). Tides are computed using the T_TIDE Matlab package (Pawlowicz et al., 2002). A harmonic analysis is conducted on GNSS-R SSH based on a list of 45 astronomical and 101 shallow-water constituents.

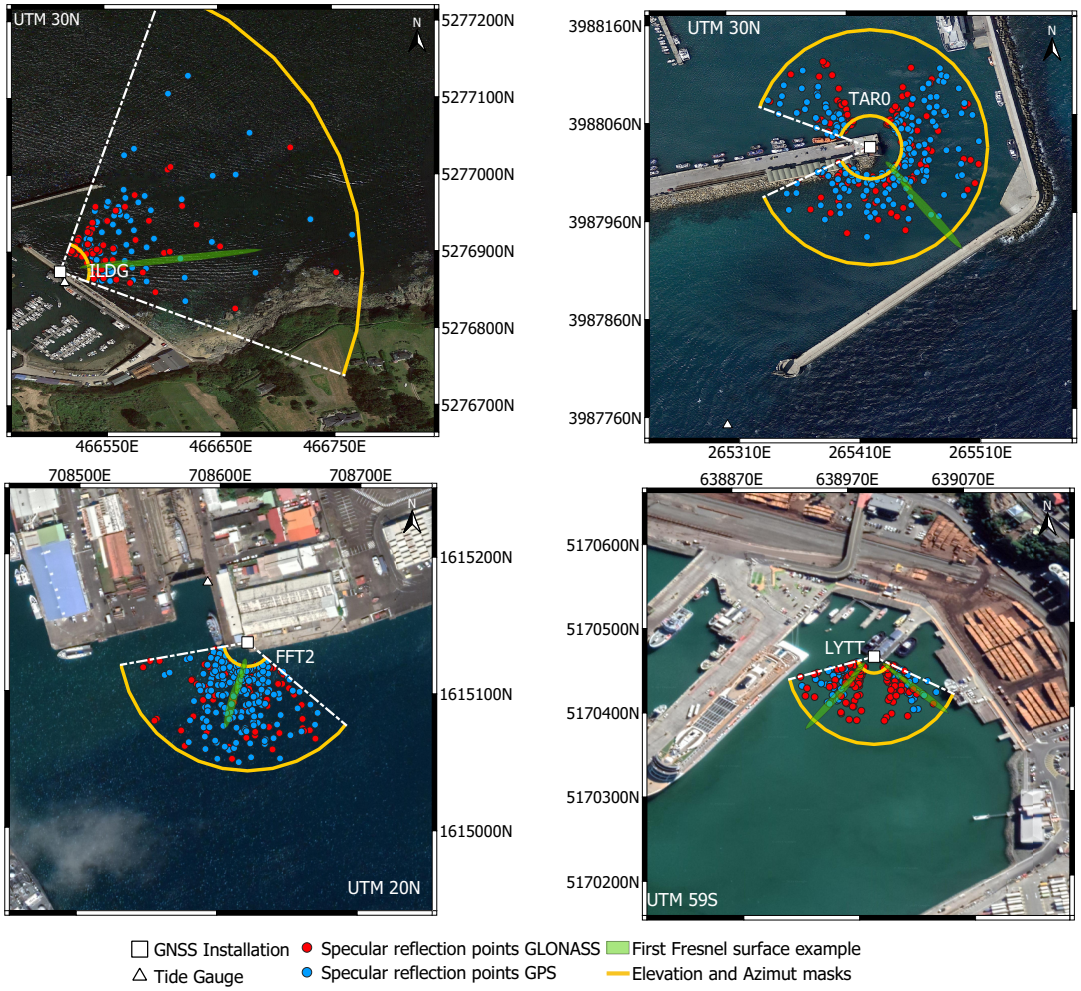

Figure 3: Position of the reflection points for each stations computed with the simulation software of Roussel et al. (2014) along with the azimut and elevation masks used in the study

An automated algorithm selects the appropriate constituents of significant amplitudes. The amplitudes and phases lags of the selected constituents are saved in a table to allow the prediction of a local tidal model. Then, GNSS-R NTR is computed as the difference between GNSS-R SSH and the tidal prediction from the local harmonic coefficients.

On the other hand, the response of sea surface to short-term atmospheric forcing is determined by the LIB approximation and DAC products. The readers are reminded here that these models have been selected as their design do not allow the estimation of other sea level variations (e.g. general circulation, coastal upwelling, local seiches, steric changes ...) when these variations cannot be separated in tide gauge measurements.

The analysis of the ocean response is made at periods of two days and longer as the LIB effect is given to have a poor signature at high frequencies (Ponte et al., 1991; Mathers and Woodworth, 2001) and as the DAC data is obtained with a 6 hours sampling, restraining the study to lower frequencies. Thus, a low-pass

filter is applied to all time series. The filtering method is based on the wavelet decomposition/reconstruction which accommodate well in case of non-stationary signals. A continuous Morse wavelet is chosen which is a complex valued wavelet (Olhede and Walden, 2002). This wavelet is convenient for analyzing signals that vary in both time and frequency. Moreover, in order to avoid seasonal variations in our time series, a similar high-pass wavelet filter is applied using a cut-off frequency of 2 months.

5. RESULTS

The analysis of the GNSS-R SSH time series consists of two points: 1) validation of the performance of our processing over a well-known ocean process, i.e. tides; 2) demonstration of the capability of the GNSS-R technique to detect other significant phenomenon as the sea surface response to atmospheric variations.

5.1. Validation of the method with tide gauges

The GNSS-R SSH estimated is compared to tide gauges measurements over one year for the 4 sites, ILDG, TAR0, FFT2 and LYTT through the harmonic analysis using T_Tide software, Pawlowicz et al. (2002). Table 2 focuses on major diurnal, semi-diurnal and quarter diurnal constituents. This comparison is based on the complex difference Δz between tide gauges records and GNSS-R estimates, for each tidal constituents defined as (e.g. Tranchant et al. (2021)):

$$\Delta z = A_{TG} e^{i\Psi_{TG}} - A_{SNR} e^{i\Psi_{SNR}} \tag{4}$$

Tide	Type	ILDG			TAR0			FFT2			LYTT		
		Amp. [cm]	Phase [°]	$\lvert\Delta z\rvert$ [cm]	Amp. [cm]	Phase [°]	$\lvert\Delta z\rvert$ [cm]	Amp. [cm]	Phase [°]	$\lvert\Delta z\rvert$ [cm]	Amp. [cm]	Phase [°]	$\lvert\Delta z\rvert$ [cm]
M2	TG	149.27	99.12	8.84	41.33	41.66	5.27	6.18	210.44	0.71	85.27	137.12	5.81
	SNR	140.35	98.75		36.05	41.75		5.48	210.09		79.46	137.14	
S2	TG	53.54	131.74	4.52	15.39	69.76	0.92	1.49	242.54	0.58	5.72	149.14	0.60
	SNR	49.33	133.53		14.47	70.21		0.92	246.48		5.14	150.57	
N2	TG	30.68	79.09	1.83	8.39	26.45	0.87	1.60	182.26	0.30	19.96	110.47	1.19
	SNR	28.81	78.16		7.53	27.52		1.41	173.58		18.83	111.52	
K2	TG	15.55	131.45	6.83	4.43	67.37	1.43	0.16	220.88	1.19	1.87	117.32	10.87
	SNR	9.97	113.01		5.13	52.30		1.03	27.47		12.62	136.50	
2N2	TG	4.10	51.55	0.62	1.12	359.29	0.41	0.44	146.79	0.16	2.99	89.09	0.60
	SNR	4.05	59.72		0.85	341.02		0.50	164.78		3.59	88.82	
K1	TG	6.36	75.44	2.09	2.59	127.58	2.11	8.66	239.52	1.39	4.64	271.00	0.68
	SNR	6.94	59.05		4.67	132.74		9.44	232.26		4.40	279.12	
01	TG	6.55	329.96	1.49	0.31	129.47	0.25	6.39	229.70	0.43	2.75	244.54	0.49
	SNR	6.47	317.37		0.46	99.33		6.02	227.70		3.17	249.20	
P1	TG	1.74	51.50	0.44	0.53	152.83	0.41	2.54	237.23	0.51	1.52	271.67	0.52
	SNR	1.35	48.39		0.74	185.45		2.63	248.30		1.89	259.39	
Q1	TG	2.03	284.69	0.65	0.51	223.97	0.09	1.20	218.16	0.32	0.96	230.21	0.23
	SNR	1.49	268.07		0.50	234.15		0.89	221.68		1.16	236.56	
M4	TG	7.35	29.60	1.15	3.83	113.13	1.79	0.19	224.51	0.07	0.33	111.15	0.64
	SNR	6.35	25.35		2.19	127.20		0.17	246.34		0.85	70.14	
MS4	TG	2.53	115.86	1.13	1.77	156.09	0.79	0.14	268.41	0.09	0.35	150.23	0.23
	SNR	2.43	141.66		1.24	179.12		0.08	231.88		0.58	155.22	
RSS		8.91			4.48			1.56			8.82		

Table 2: Usual tide constituents derived from the tide gauge observations and the GNSS-R measurements for each sites. TG: Tide Gauge, SNR: GNSS-R SNR method, RSS: Root-Sum-Square in cm

with A the amplitude and Ψ the phase of the corresponding tidal constituents. A Root-Sum-Square (RSS) based on these differences gives the combined error derived from individual tidal constituent:

$$RSS = \sqrt{\frac{1}{2} \sum_{constituents} |\Delta z|^2} \tag{5}$$

For each site, the harmonic analysis gives good results with a RSS less than 3% of the site tidal range, featuring acceptable amplitude discrepancies and good agreement for phase lags. The RSS increases with the tidal range of the site, ranging from a centimeter order in a micro tidal environment at FFT2 to a decimeter order in a macrotidal environment.

While considering the 4 sites, the amplitude error is always less 5% of the site tidal range. There is almost no phase lags differences (always smaller than 5°), leading to small differences $|\Delta z|$ with the tide gauge (less than 11 cm). The differences on these major constituents explain most of the RSS value. For example, at ILDG and TAR0, the biggest difference is seen on the major astronomical constituent M2. This is similarly observed for almost every significant tidal constituents (e.g. S2, N2, ...) in the 4 sites. The $|\Delta z|$ is related to the amplitude of the constituent itself with an underestimation of the GNSS-R tidal constituent. This appears to be the signature of the absence of tropospheric corrections, which induce a scaling factor (Williams and Nievinski, 2017; Peng et al., 2019) on the GNSS-R estimates.

There are however some exceptions with the $|\Delta z|$ on the K1 and K2 constituents. This illustrates a general issue: for the lunar diurnal constituent K1 and especially for the lunisolar semi-diurnal constituent K2, the discrepancy on phase lags is significant regarding the amplitude of the constituent (18° for ILDG for the K2). This phenomenon has been observed by Tabibi et al. (2020); Larson et al. (2017) and is correlated to the period of GPS orbit of 11.97 hours. Consequently, this leads to errors on both K1 and K2 constituents and significant contributions in the total error budget.

These results validate the performance of GNSS-R to observe first order sea level variations, as the tides correspond to most of sea level variations signal. For instance, the tide model represent 96% of the GNSS-R SSH time series variability for ILDG in terms of standard deviation. Consequently, global Pearson correlation between the GNSS-R time series and tide gauge measurements is really good, ranging from 0.91 at FFT2 to 0.97 at ILDG and TAR0. Still, other phenomena are present in the GNSS-R time series. For this purpose, NTR are computed by removing the tidal height predictions from GNSS-R SSH (see section 4).

5.2. GNSS-R Non-Tidal Residual at short time scales

The GNSS-R NTR are first directly compared to times series derived from LIB and DAC. The correlation coefficients are computed before and after application of a band-pass filter of 2 days to 2 months, (Lyard and Roblou, 2003). Figure 4 shows that bandpass filtered data are generally better correlated. For ILDG, TAR0 and LYTT the correlation between GNSS-R and LIB (respectively DAC) increases of 0.47, 0.28 and 0.47 (respectively 0.44, 0.32 and 0.49) after filtering. These results agree with the fact that the sea level response to atmospheric forcing is a dynamic phenomenon that differs from the IB approximation at subtidal time

scales till 2 months (Carrère, 2003; Lyard and Roblou, 2003). Analyzing the filtered series, the correlation values between GNSS-R NTR and meteorological forcing models are above 0.6 (see Figure 4 and Figure 5) confirming significant signatures of meteo-driven sea level variation in the GNSS-R observations. However, in the case of FFT2, the NTR is uncorrelated with LIB or DAC even after filter application, since the correlation values are below 0.5.

Filtered time series of GNSS-R NTR, LIB and DAC (Figure 5) show similar variability and trends (e.g. a RMS of about 0.1 m for the three time series at ILDG). We notice that there are significant discrepancies in NTR variability for the 4 sites. The lowest variability is for FFT2 site (RMS of NTR of 0.03 m) and the highest ILDG (RMS of NTR of 0.115 m). The meteo-driven sea level variations in FFT2 are of the order of the GNSS-R resolution (with accuracy of 1 to 3 cm), explaining the low correlation values with respect to LIB and DAC. In the case of ILDG and TAR0, the NTR signal variability exhibit a significant temporal

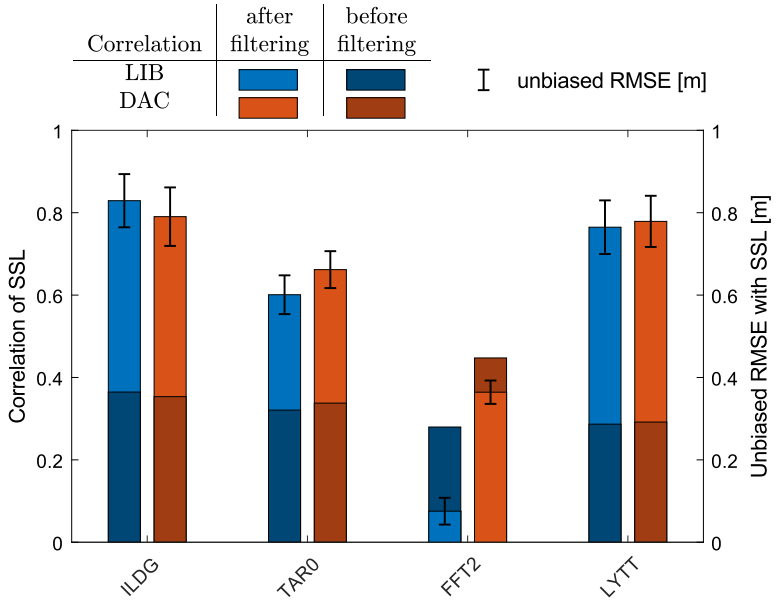

Figure 4: Pearson correlation between the NTR and both the LIB and DAC models before and after the application of the filters. RMSE between the time series are represented through the form of error bars

	ILDG	TAR0	FFT2	LYTT
NTR correlation with LIB				
BF	0.36	0.32	0.28	0.29
AF	0.83	0.60	0.08	0.76
NTR correlation with DAC				
BF	0.35	0.34	0.45	0.29
AF	0.79	0.66	0.36	0.78

BF: before filtering
AF: after filtering

Table 3: Numerical values of the Pearson correlation between NTR and both LIB and DAC before and after the application of a bandpass filter

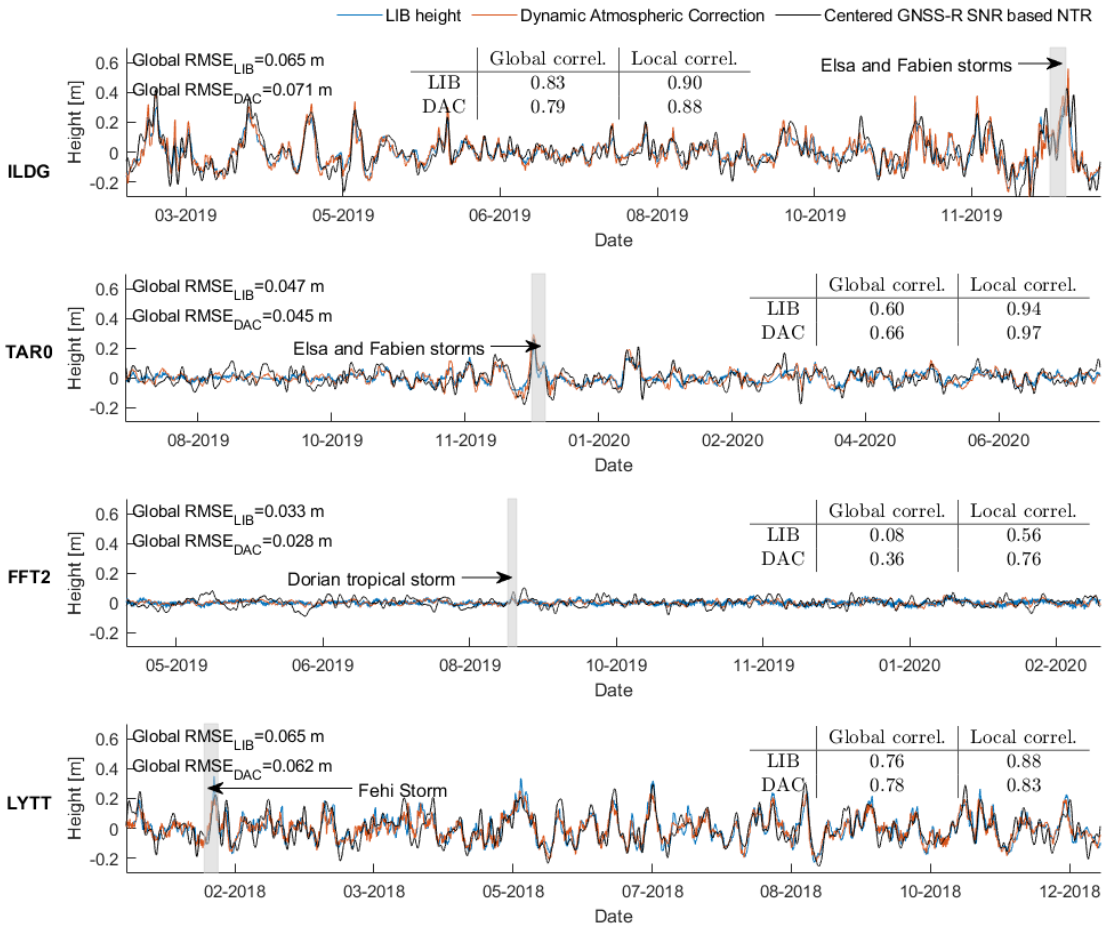

Figure 5: Time series of the NTR in black and both LIB height in blue and DAC in red for each sites. The greyed zones correspond to important meteorological phenomena. Here global refers to the whole time series while local refers the highlighted stormy period.

variability. In fact, in 2019, NTR variations are smaller during the summer than in winter (the NTR RMS is multiplied by 2.84 from the summer to the winter at ILDG).

We also focus on large variations during storms. The local correlations are in the 0.6-0.9 interval considering only storms with durations larger than a few days (Figure 5), demonstrating the presence of the signature in GNSS-R NTR times series of the sea level variations caused by storms. The NTR signal presents a great non-stationary behavior. Thus, to provide further analysis, crosswavelet coherence maps using XWT (Grinsted et al., 2004) are computed between NTR, LIB and DAC (Figure 6). The coherence maps show large differences between the 4 sites. In the case of ILDG and LYTT, a wide range of frequencies (2-32 days or 2-64 days) reveals a good coherence. The coherence map of TAR0 displays a strong variability. At FFT2, high coherence values are in the band of 4-8 days only. During the 2019 summer, the ILDG and TAR0

maps present a drop in coherence corresponding to periods of weak atmospheric activity. Storm periods are highlighted in the coherence maps (Figure 6) presenting high values at periods lower than 1-2 weeks.

Above the 20-days threshold, the coherences obtained with the LIB and the DAC are the same (as both models are constructed on the same approximation for these longer periods). Differences can be seen at periods smaller than 20 days where the LIB leads to lower coherence values than the DAC.

6. DISCUSSION

The main goal of the study is to assess the capability of the GNSS-R to independently retrieve sea level variations other than the tides, with a focus on the response to short-term meteorological forcing. Before studying in depth the non-tidal parts of this retrieved sea level, we verify that our estimates are good enough for the study. Correlations between the GNSS-R derived sea level and tide gauge measurements ranges from 0.91 at FFT2 to 0.97 at ILDG. These values are consistent with the ones previously found in studies comparing GNSS-R and tide gauge data (Roussel et al. (2015); Vu et al. (2019); Geremia-Nievinski et al. (2020)). These outcomes are quite trivial as tides represent the ultra-dominant part of the sea level in the selected stations.

Table 2 presents a comparison between the tidal analysis of GNSS-R estimates and tide gauge records as previously done by Larson et al. (2017),Tabibi et al. (2020) and Löfgren et al. (2014). The complex differences on the major tidal constituents ranges from several millimeters to about a decimeter (i.e. at ILDG for the M2, with a complex error amplitude of 8.84 cm). Löfgren et al. (2014) previously found amplitude differences of the same order with a $|\Delta z|$ of 14.79 cm at Burnie, Australia, for the M2 component. This estimate remains also coherent with the results of Tabibi et al. (2020) with RSS ranging from less than a decimeter to a few centimeters depending upon the site. In our case, the relative errors with respect to the harmonic amplitude at tide gauge, A_{TG}, are consistent for all the major harmonic constituents except for K2 (and inherently K1), which frequency (11.97 hours) is close to the one of GPS sidereal period (Tabibi et al., 2020). Larson et al. (2017) suspected possible biases on the estimates at K1 due to the GPS orbital period. Such discrepancies are similarly found here in meso to macrotidal conditions as in ILDG for instance. Although this issue has been observed in several GNSS-R studies (Tabibi et al., 2020; Larson et al., 2017), unfortunately it has never been characterized. This issue impacts every GNSS-based technique and the effects of the different constellations on these biases are the object of studies in classical GNSS methods (Matviichuk et al., 2020; Abbaszadeh et al., 2020).

The comparison of the tide gauge constituents and those from the GNSS-R shows that the reflectometry leads to an underestimation of the constituents amplitude and errors in phase lag. This issue is pointed out in the methodology and is due to the lack of tropospheric corrections in the processing. Table 2 shows as wall that the RSS tends to decrease with the tidal range. The same feature has been previously observed by Löfgren et al. (2014) by comparing the error at tide gauges and the tidal range for five different stations.

The RSS obtained are in good agreement with the results of similar studies (Löfgren et al., 2014; Tabibi

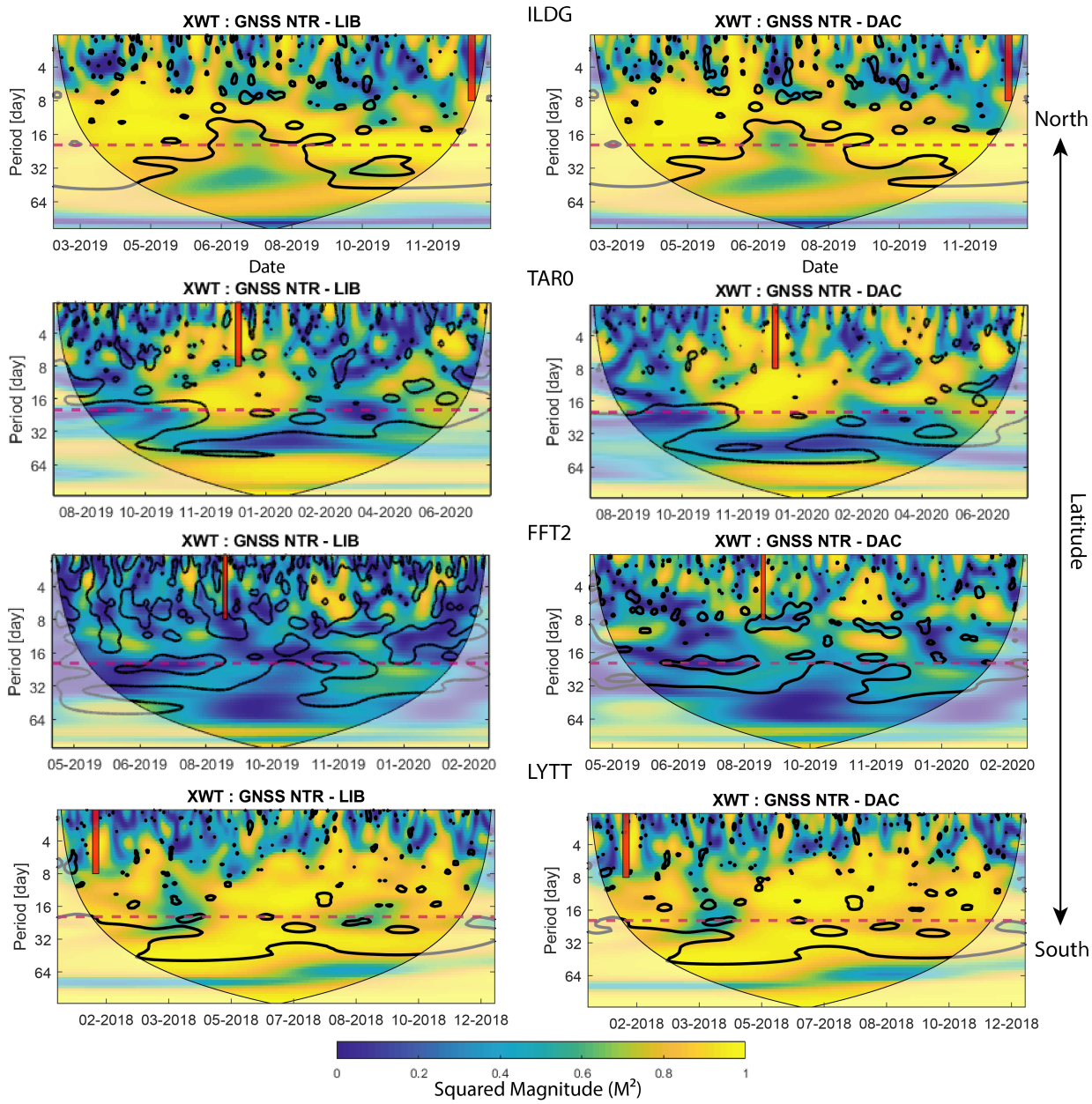

Figure 6: Wavelet cross correlation maps between the NTR and both LIB (on the left column) and DAC (on the right column) time series for each sites on the left; a 5% significance level against noise is shown through the thick contour. The different storms considered in the study are represented on the map in red. The horizontal line is set at 20 days, the threshold above which the DAC is based on a barotropic model and under which it is goes back to the IB approximation

et al., 2020) (about a decimeter in macro-tidal and less in micro-tidal environment) and most of the difference can be explained due to a loose estimate of K2 constituent at ILDG and LYTT sites, explaining about half of the total RSS at LYTT and 23% at ILDG. Do note that any errors in determining tides using a classical harmonic analysis has no impact when predicting the tidal model applying those same (erroneous)

harmonic coefficients (e.g. Pawlowicz et al. (2002)). So, the computed NTR are poorly impacted by observed discrepancies at tidal periods. The non-tidal part of the sea level is then compared to independent models of the sea level response to meteorological forcing, namely LIB and DAC.

Tides represent 96% of the total GNSS-R estimate variability at ILDG. In the following, we will focus on the residual part of the sea level signal once tides are removed. Historically, the weather impact on the sea level was explained using the LIB model. The comparison of the NTR with the LIB was conducted here as a first step. As the comparisons are already good with the LIB model, a more valid but complex model was used: the Dynamic Atmospheric Correction. For short periods, the comparison of the NTR time series with the DAC will prevail as it is a better approximation of the weather-induced variations of the sea level than the LIB (Carrère, 2003).

ILDG and LYTT show similar NTR time series as these stations are located in a macro to meso-tidal environment with similar meteorological behaviour. Figure 5 presents the sea surface response to atmospheric forcings at these two sites, where a good correlation exists between NTR and the two sea level models. For both sites, the correlation is above 0.6. This value is similar to the correlation factor of 0.7 previously observed by Vu et al. (2019) at the Socoa site in the bay of Biscay. Bandpass filtering between 2 days and 2 months of the time series increase the correlation from 0.44 at ILDG to 0.49 at LYTT (see Figure 4). The ILDG and LYTT coherence maps (see Figure 6) are also similar for the complete time series, in particular for periods between 4 to 32-64 days, and show discrepanties for shorter periods (2-4 days). It is consistent with the idea that the LIB model behaves poorly at periods lower than 2 days (Ponte, 1993)). Moreover, temporal interruptions of coherence occur, e.g. for the ILDG station in summer 2019, when the Azores High is located closer to Europe, reducing the number of weather cyclonic systems approaching the coasts.

The impact of the atmospheric variations on the sea surface height is also observed at TAR0 with correlations higher than 0.6. For this latter station, the filtering increases the correlation to a minor extent compared to ILDG and LYTT (increase of 0.28 and 0.32 for both LIB and DAC) due to the lack of average signal power at periods greater than 2 days. The impact of the atmospheric variations on the sea level is obvious for TAR0 (see Figure 6) during the complete observation period, except for August-October 2019 with the same atmospheric low activity phenomenon than for ILDG. FFT2 corresponds to the worst case with a correlation of less than 0.4 even if the signature of meteorological effects is however revealed by the coherence map: high coherence values are being obtained for periods of 4-8 days related to important atmospheric events.

When the atmospheric variations are large, their effects are more detectable in the GNSS-R NTR time series. For instance, in ILDG and LYTT stations, the NTR RMS is of about 0.1 m for both model : 9 cm for the LIB for both stations and respectively 10 and 8 cm for the DAC. The RMS are less for TAR0 and FFT2, i.e. of 0.04 m and 0.01 m for both models.

This behaviour is confirmed by the study of specific meteorological events. Two examples of noteworthy atmospheric events are observable in our time series. The first one is based on storms which induces great

sea level variations as illustrated by an increase of the DAC RMS. For instance, at ILDG, the DAC RMS increases from 0.10 m on the whole time series to 0.275 m during storms events. ILDG is taken as example but the behaviour is typical and observable at the other sites. These periods of strong meteorological activity translate into high correlation with the sea level increase of variability. Vu et al. (2019) observed an increase of correlation of 0.3 during the storm Xynthia. However, in our study, even larger increases are observed for each sites. The second example consists in the position of the Azores High itself. During the 2019 summer (July to September), a drop on the coherence map is observed at ILDG and TAR0. It is also visible on the time series with a decreasing DAC RMS (0.10 m on the whole time series to 0.064 m during 2019 summer at ILDG). During this specific period, the Azores high was located closer to Europe, reducing the number and intensity of the atmospheric systems reaching the coasts.

GNSS reflectometry allows the retrieval of sea level whose detided signal is dynamically forced by several phenomena, among them the atmospheric pressure and the wind effect. As the pressure effect is only predominant at low frequencies, an isostatic response of the sea level to barometric variation is not totally suited for coastal high frequencies sea level analysis. This inability of the LIB to describe high-frequency sea level variations is pointed by the comparison with the GNSS-R product as the DAC shows much more coherence above the 20 days threshold with the non-tidal GNSS-R residual.
The signature of the meteo-induced variations in NTR is observed on the coherence map on a wide spectrum of frequencies, from a few days to months in agreement with both the LIB and DAC models. This shows the capability of the GNSS-R technique to reveal these phenomena.

7. CONCLUSION

The GNSS-R SNR technique is used to produce yearly time series of the sea level variations at four sites located at different latitudes. This study tackles two points:
1) A first validation step consists in a tidal analysis intercomparison of GNSS-R profiles and records from tide gauges stations in the neighbourhood of those sites. Small Root-Sum-Square errors (under 10 cm) are obtained validating our GNSS-R SNR estimates. 2) Then, the NTR is compared to the LIB and the DAC, two analytical and numerical models. This comparison conducted at periods between 2 days and 2 months, leads to correlations greater than 0.6 , even reaching 0.9 during noteworthy atmospheric events such as intense cyclonic events. These results at ILDG, TAR0 and LYTT highlight the signature of short-term meteorological forcing in GNSS-R sea level estimates in most situations. However, located at the lowest latitude, the FFT2 station represents the typical case of small and steady atmospheric activity. Consequently, the corresponding time series estimated by GNSS-R is hardly correlated to atmospheric forcing. The FFT2 sea level is probably affected by other local effects.
Overall, the GNSS-R technique itself can be used to measure tides variations at first order with enhanced results when tropospheric corrections are made. Moreovoer, this technique has shown here the capability

to produce Non-Tidal Residual estimates suited for studying the impact of specific forcing factors affecting sea level. In order to reach and thus understand the lower order coastal phenomena affecting sea level, the 2-3 centimeters accuracy of the GNSS-R needs to be improved. For this purpose, new positioning satellite constellations, such as Galileo, Beidou, QZSS and IRNSS, would be included in the SNR determination of sea surface level if they are available. This should also mitigate the error due to the K1/K2 tidal constituents. The impact of different constellations orbit geometrics on the K1/K2 tidal constituents has to be further studied in GNSS-R, as it has already be done with PPP methods (Matviichuk et al., 2020).

Besides the improvements on the GNSS-R, the two models used to compute the specific response of the sea level to weather variations can also be improved for coastal applications. Indeed, while the DAC and LIB are identical for periods greater than 20 days, the former is preferred for shorter periods as it takes into account the effects of the wind forcing. However the DAC suffers from a coarse spatial resolution of 0.25° and a poor temporal resolution (6 hours), that makes any accurate local comparison with GNSS-R time series difficult. To help calibrate of validate these models, the GNSS reflectometry could be used through the production of verification data-sets, similarly to what is routinely done with tide gauges.

Once a proper reduction of meteorologically-induced contribution is achieved, the remaining sea level variations, could be observed. As the sea level variations have been filtered in a 2-day to 2-month window, a non negligible quantity of forcing factors have been omitted. Investigating further these other variations is a real opportunity for coastal characterization. For example, Peng et al. (2021) has recently presented clear observation of seasonal sea level variations.

Acknowledgement

We aknowledge funding from the foundation of Thematic Network for Advanced Research (RTRA) in Science and Technology for Aeronautics and space (STAE) under the SVD-ENV project. We thank the SONEL service for the GNSS data distribution. Finally, we thank the two anonymous reviewers for their valuable comments.

References

Abbaszadeh, M., Clarke, P.J., Penna, N.T., 2020. Benefits of combining gps and glonass for measuring ocean tide loading displacement. Journal of Geodesy 94, 1–24.

Ablain, M., Legeais, J., Prandi, P., Marcos, M., Fenoglio-Marc, L., Dieng, H., Benveniste, J., Cazenave, A., 2017. Satellite altimetry-based sea level at global and regional scales. Surveys in Geophysics 38, 7–31.

Anzidei, M., Scicchitano, G., Scardino, G., Bignami, C., Tolomei, C., Vecchio, A., Serpelloni, E., De Santis, V., Monaco, C., Milella, M., et al., 2021. Relative sea-level rise scenario for 2100 along the coast of South Eastern Sicily (Italy) by InSAR data, satellite images and high-resolution topography. Remote Sensing 13, 1108.

Bishop, G., Klobuchar, J., Doherty, P., 1985. Multipath effects on the determination of absolute ionospheric time delay from GPS signals. Radio Science 20, 388–396.

Carrère, L., 2003. Etude et modélisation de la réponse haute fréquence de l'océan global aux forçages météorologiques. Ph.D. thesis. Toulouse 3.

Carrere, L., Faugère, Y., Ablain, M., 2016. Major improvement of altimetry sea level estimations using pressure-derived corrections based on ERA-Interim atmospheric reanalysis. Ocean Science 12, 825–842.

Carrère, L., Lyard, F., 2003. Modeling the barotropic response of the global ocean to atmospheric wind and pressure forcing-comparisons with observations. Geophysical Research Letters 30.

Chen, F., Liu, L., Guo, F., 2019. Sea surface height estimation with multi-GNSS and wavelet de-noising. Scientific reports 9, 1–10.

Cipollini, P., Benveniste, J., Birol, F., Fernandes, M.J., Obligis, E., Passaro, M., Strub, P.T., Valladeau, G., Vignudelli, S., Wilkin, J., 2017. Satellite altimetry in coastal regions, in: Satellite altimetry over oceans and land surfaces. CRC Press, pp. 343–380.

Ding, Y., Yu, H., Bao, X., Kuang, L., Wang, C., Wang, W., 2011. Numerical study of the barotropic responses to a rapidly moving typhoon in the East China Sea. Ocean Dynamics 61, 1237.

García, M.J., Molinero, J., 2006. Estación mareográfica de Tarifa. Inst. Esp. de Oceanogr., Madrid.(Available at www. ieo. es/indamar/mareas/documentos/informe-estadisticas-tarifa. pdf.) .

Geremia-Nievinski, F., Hobiger, T., Haas, R., Liu, W., Strandberg, J., Tabibi, S., Vey, S., Wickert, J., Williams, S., 2020. SNR-based GNSS reflectometry for coastal sea-level altimetry: results from the first IAG inter-comparison campaign. Journal of Geodesy 94, 1–15.

Gregory, J.M., Griffies, S.M., Hughes, C.W., Lowe, J.A., Church, J.A., Fukimori, I., Gomez, N., Kopp, R.E., Landerer, F., Le Cozannet, G., et al., 2019. Concepts and terminology for sea level: Mean, variability and change, both local and global. Surveys in Geophysics 40, 1251–1289.

443 Grinsted, A., Moore, J.C., Jevrejeva, S., 2004. Application of the cross wavelet transform and wavelet
444 coherence to geophysical time series. Nonlinear processes in geophysics 11, 561–566.

445 Larson, K.M., Löfgren, J.S., Haas, R., 2013. Coastal sea level measurements using a single geodetic GPS
446 receiver. Advances in Space Research 51, 1301–1310.

447 Larson, K.M., Ray, R.D., Williams, S.D., 2017. A 10-year comparison of water levels measured with a
448 geodetic GPS receiver versus a conventional tide gauge. Journal of Atmospheric and Oceanic Technology
449 34, 295–307.

450 Larson, K.M., Small, E.E., Gutmann, E., Bilich, A., Axelrad, P., Braun, J., 2008. Using GPS multipath to
451 measure soil moisture fluctuations: initial results. GPS solutions 12, 173–177.

452 Löfgren, J.S., Haas, R., Scherneck, H.G., 2014. Sea level time series and ocean tide analysis from multipath
453 signals at five GPS sites in different parts of the world. Journal of Geodynamics 80, 66–80.

454 Lomb, N.R., 1976. Least-squares frequency analysis of unequally spaced data. Astrophysics and space science
455 39, 447–462.

456 Lyard, F., Roblou, L., 2003. Prévision de produit combine du niveau de la mer en Méditerranée 25–
457 comparaisons avec des observations. La letter trimestrielle de MERCATOR 10, 17–27.

458 Mathers, E., Woodworth, P., 2001. Departures from the local inverse barometer model observed in altimeter
459 and tide gauge data and in a global barotropic numerical model. Journal of Geophysical Research: Oceans
460 106, 6957–6972.

461 Matviichuk, B., King, M., Watson, C., 2020. Estimating ocean tide loading displacements with gps and
462 glonass. Solid Earth 11, 1849–1863.

463 Melet, A., Teatini, P., Le Cozannet, G., Jamet, C., Conversi, A., Benveniste, J., Almar, R., 2020. Earth
464 observations for monitoring marine coastal hazards and their drivers. Surveys in Geophysics 41, 1489–1534.

465 Meli, M., Olivieri, M., Romagnoli, C., 2021. Sea-level change along the Emilia-Romagna coast from tide
466 gauge and satellite altimetry. Remote Sensing 13, 97.

467 Olhede, S.C., Walden, A.T., 2002. Generalized morse wavelets. IEEE Transactions on Signal Processing 50,
468 2661–2670.

469 Pawlowicz, R., Beardsley, B., Lentz, S., 2002. Classical tidal harmonic analysis including error estimates in
470 MATLAB using T_TIDE. Computers & Geosciences 28, 929–937.

471 Peng, D., Feng, L., Larson, K.M., Hill, E.M., 2021. Measuring coastal absolute sea-level changes using gnss
472 interferometric reflectometry. Remote Sensing 13, 4319.

473 Peng, D., Hill, E.M., Li, L., Switzer, A.D., Larson, K.M., 2019. Application of GNSS interferometric reflec-
474 tometry for detecting storm surges. GPS Solutions 23, 1–11.

475 Pérez, B., Payo, A., López, D., Woodworth, P., Alvarez Fanjul, E., 2014. Overlapping sea level time series
476 measured using different technologies: an example from the REDMAR Spanish network. Natural Hazards
477 and Earth System Sciences 14, 589–610.

478 Ponte, R.M., 1993. Variability in a homogeneous global ocean forced by barometric pressure. Dynamics of
479 atmospheres and oceans 18, 209–234.

480 Ponte, R.M., Carson, M., Cirano, M., Domingues, C.M., Jevrejeva, S., Marcos, M., Mitchum, G., Van De Wal,
481 R., Woodworth, P.L., Ablain, M., et al., 2019. Towards comprehensive observing and modeling systems
482 for monitoring and predicting regional to coastal sea level. Frontiers in Marine Science 6, 437.

483 Ponte, R.M., Salstein, D.A., Rosen, R.D., 1991. Sea level response to pressure forcing in a barotropic
484 numerical model. Journal of physical oceanography 21, 1043–1057.

485 Remus, R., Aguado-Monsonet, M.A., Roudier, S., Delgado Sancho, L., 2010. JRC reference report. Best
486 Available Techniques (BAT) Reference Document for Iron and Steel Production, Industrial Emissions
487 Directive 75.

488 Roden, G.I., Rossby, H.T., 1999. Early swedish contribution to oceanography: Nils gissler (1715–71) and the
489 inverted barometer effect. Bulletin of the American Meteorological Society 80, 675–682.

490 Ross, J.C., 1854. XII. on the effect of the pressure of the atmosphere on the mean level of the ocean.
491 Philosophical Transactions of the Royal Society of London , 285–296.

492 Roussel, N., Frappart, F., Ramillien, G., Darrozes, J., Desjardins, C., Gegout, P., Pérosanz, F., Biancale,
493 R., 2014. Simulations of direct and reflected wave trajectories for ground-based GNSS-R experiments.
494 Geoscientific Model Development 7, 2261–2279.

495 Roussel, N., Ramillien, G., Frappart, F., Darrozes, J., Gay, A., Biancale, R., Striebig, N., Hanquiez, V.,
496 Bertin, X., Allain, D., 2015. Sea level monitoring and sea state estimate using a single geodetic receiver.
497 Remote sensing of Environment 171, 261–277.

498 Santamaría-Gómez, A., Watson, C., 2017. Remote leveling of tide gauges using gnss reflectometry: case
499 study at spring bay, australia. GPS solutions 21, 451–459.

500 Santamaría-Gómez, A., Watson, C., Gravelle, M., King, M., Wöppelmann, G., 2015. Levelling co-located
501 gnss and tide gauge stations using gnss reflectometry. Journal of Geodesy 89, 241–258.

502 Shukla, J., Verma, M., Misra, A., 2017. Effect of global warming on sea level rise: A modeling study.
503 Ecological Complexity 32, 99–110.

Smyrnaios, M., Schn, S., Liso, M., Jin, S., 2013. Multipath propagation, characterization and modeling in GNSS. Geodetic sciences-observations, modeling and applications , 99–125.

Tabibi, S., Geremia-Nievinski, F., Francis, O., van Dam, T., 2020. Tidal analysis of GNSS reflectometry applied for coastal sea level sensing in Antarctica and Greenland. Remote Sensing of Environment 248, 111959.

Tranchant, Y.T., Testut, L., Chupin, C., Ballu, V., Bonnefond, P., 2021. Near-coast tide model validation using GNSS unmanned surface vehicle (USV), a case study in the Pertuis Charentais (France). Remote Sensing 13, 2886.

Vignudelli, S., Cipollini, P., Roblou, L., Lyard, F., Gasparini, G., Manzella, G., Astraldi, M., 2005. Improved satellite altimetry in coastal systems: Case study of the corsica channel (mediterranean sea). Geophysical Research Letters 32.

Vinogradova, N.T., Ponte, R.M., Stammer, D., 2007. Relation between sea level and bottom pressure and the vertical dependence of oceanic variability. Geophysical research letters 34.

Voineson, G., 2013. Le réseau d'observation du niveau de la mer du SHOM: RONIM .

Vu, P.L., Ha, M.C., Frappart, F., Darrozes, J., Ramillien, G., Dufrechou, G., Gegout, P., Morichon, D., Bonneton, P., 2019. Identifying 2010 Xynthia storm signature in GNSS-R-based tide records. Remote Sensing 11, 782.

Williams, S., Nievinski, F., 2017. Tropospheric delays in ground-based gnss multipath reflectometry—experimental evidence from coastal sites. Journal of Geophysical Research: Solid Earth 122, 2310–2327.

Woodworth, P., 1991. The permanent service for mean sea level and the global sea level observing system. Journal of Coastal Research , 699–710.

Woodworth, P.L., Melet, A., Marcos, M., Ray, R.D., Wöppelmann, G., Sasaki, Y.N., Cirano, M., Hibbert, A., Huthnance, J.M., Monserrat, S., et al., 2019. Forcing factors affecting sea level changes at the coast. Surveys in Geophysics 40, 1351–1397.

Wöppelmann, G., 2004. SONEL–Système d'Observation du Niveau des Eaux Littorales. Actes de l'atelier Expérimentation et Instrumentation IFREMER, INSU, Météo-France, Paris , 23–24.

Wunsch, C., Stammer, D., 1997. Atmospheric loading and the oceanic "inverted barometer" effect. Reviews of Geophysics 35, 79–107.

List of Figures